

IRAS 16475–4609: A Young Compact HII Region Sculpting Its Molecular Environment

FELIPE NAVARETE ^{1,2} SEAN D. POINTS ³ AND AUGUSTO DAMINELI ⁴

¹*Laboratório Nacional de Astrofísica, Rua dos Estados Unidos 154, 37504-364, Itajubá, MG, Brazil*

²*NSF's NOIRLab/SOAR Telescope, Casilla 603, La Serena, 1700000, Chile*

³*NSF's NOIRLab/CTIO, Casilla 603, La Serena, 1700000, Chile*

⁴*Instituto de Astronomia, Geofísica e Ciências Atmosféricas da USP, Rua do Matão 1226, Cidade Universitária, São Paulo, Brasil*

(Received February 20, 2025; Revised May 27, 2025; Accepted June 11, 2025)

Submitted to AJ

ABSTRACT

We present a near-infrared spectroscopic and imaging analysis of the star-forming region IRAS 16475–4609, based on TripleSpec/SOAR spectroscopy and NEWFIRM/CTIO imaging, complemented by archival radio and sub-millimeter data. Our spectroscopic analysis indicates that the central source is an early B-type star (B0-B0.7 V) powering a compact H II region characterized by strong H I and He I recombination lines, and molecular H₂ emission. We derive a distance of 3.51 ± 0.74 kpc, consistent with the position of the Scutum-Crux near arm at Galactic longitudes of $\sim 340^\circ$. At this distance, the ionized gas traced by Br γ emission has a radius of 0.27 ± 0.06 pc, placing the source in a transition phase between ultra-compact and compact H II regions. From radio data, we estimate an ionizing photon flux of $N_{I\gamma} = (2.3 \pm 0.3) \times 10^{47}$ photons s⁻¹, and an electron temperature of $T_e = (5.4 \pm 0.2) \times 10^3$ K for the ionized gas. The analysis also reveals an obscured high-density molecular clump southwest of the H II region, coincident with an ATLASGAL sub-millimeter peak, indicating a potential site of ongoing and triggered star formation as the ionization front advances into the surrounding molecular material. These results suggest that IRAS 16475–4609 is a young high-mass star-forming region with stellar feedback actively shaping its environment, offering valuable insight into the early evolution of compact H II regions.

Keywords: stars: massive – stars: distances – (ISM:) HII regions – ISM: individual objects (IRAS 16475-4609) – techniques: spectroscopic

1. INTRODUCTION

High-mass star formation plays a fundamental role in shaping the structure and evolution of the interstellar medium (ISM). Throughout their lives, these stars significantly impact their surroundings, emitting intense ultraviolet (UV) radiation, driving powerful stellar winds, and eventually exploding as supernovae, providing feedback mechanisms for subsequent and triggered star formation (Lada 1987) and the overall dynamics of the Galaxy. During their early stages, high-mass stars ionize their immediate environment, creating compact H II regions within the dense molecular clouds from which they formed (Wood & Churchwell 1989a). H II re-

gions are not only crucial for understanding the physical conditions around young stars but are also among the most prominent tracers of star-forming regions and the spiral structure of the Galaxy (Moisés et al. 2011; Hou & Han 2014).

In particular, the ultra-compact H II region (UCH II) represents the earliest observable phase of this process, characterized by small sizes (≤ 0.1 pc), high electron densities (10^4 – 10^5 cm⁻³), and strong free-free radio emission (Kurtz 2005). As the spectral energy distribution of UCH IIs peaks in the far-infrared (FIR), they have historically been identified through their characteristic FIR colors from large-scale surveys such as IRAS and Spitzer (Wood & Churchwell 1989a; Mottram et al. 2010). Indeed, Wood & Churchwell (1989b) identified UCH II candidates based on FIR flux density (F_λ) ratio criteria, with $\log(F_{25\mu m}/F_{12\mu m}) > 0.57$ and

$\log(F_{60\mu\text{m}}/F_{12\mu\text{m}}) > 1.3$, which serve as robust indicators of dense, dusty environments typically surrounding young high-mass stars.

Despite the critical role of young H II regions in high-mass star formation, many of these regions remain poorly characterized, limiting our understanding of their physical conditions and evolutionary states. One such example is IRAS 16475–4609, a source that has been only superficially investigated in previous surveys. Located at Galactic coordinates $\ell=339^\circ.72$, $b=-1^\circ.20$, slightly away from the densest regions of the Galactic plane and in the vicinity of well-known high-mass star-forming regions such as RCW 106 ($d = 3.5\text{--}4.0$ kpc, [Russeil 2003](#); [Moisés et al. 2011](#)), G339.88–1.26 ($d = 2.8\pm0.5$ kpc, [Green et al. 2017](#)), and West-erlund 1 ($d = 4.05\pm0.20$ kpc, [Navarete et al. 2022](#)), IRAS 16475–4609 has the potential to provide insights into the interaction between molecular clouds and ionizing radiation from high-mass stars.

The FIR colors of IRAS 16475–4609 – $\log(F_{25\mu\text{m}}/F_{12\mu\text{m}}) = 0.7$ and $\log(F_{60\mu\text{m}}/F_{12\mu\text{m}}) = 1.5$ – are consistent with the expected UCH II thresholds from [Wood & Churchwell \(1989b\)](#), reinforcing its classification as a candidate UCH II region surrounded by a dense and dusty environment. The detection of 6.668-GHz methanol maser emission represents another key observational signature of the earliest phases of high-mass star formation, as such masers are typically associated with young, deeply embedded massive protostars ([Menten 1991](#); [Urquhart et al. 2013](#)). For IRAS 16475–4609, positive methanol maser detection was reported by [Walsh et al. \(1995\)](#) but subsequent observations by [Walsh et al. \(1997\)](#) did not confirm this emission, suggesting variability or a transient nature of the maser.

Additionally, IRAS 16475–4609 has been identified as a diffuse H II region (G339.7178–01.2089) in the Red MSX Source survey ([Lumsden et al. 2013](#)) and classified as a P-type object based on its low-resolution mid-infrared spectral properties ([Kwok et al. 1997](#)). The presence of polycyclic aromatic hydrocarbon (PAH) emission features, characteristic of star-forming regions, points to a dense and dusty environment around the source, consistent with the conditions expected for a young H II region.

While the combined evidence from FIR colors, methanol maser variability, and mid-infrared spectral properties suggests that IRAS 16475–4609 hosts a young, massive star embedded in a dense molecular cloud, these observations lack the spatial and spectral resolution needed to resolve the detailed physical structure of the ionized and molecular gas. Thus, higher an-

gular resolution is essential to disentangle compact ionized emission from surrounding extended nebular or continuum components, allowing a clearer characterization of the H II region morphology and its interaction with the molecular environment. Furthermore, high spectral resolution enables accurate measurement of line profiles and radial velocities, which are crucial for determining a reliable distance estimate and, consequently, better constrain the location of IRAS 16475–4609 within the Galaxy.

To address these limitations, this work presents a comprehensive analysis of IRAS 16475–4609 using near-infrared (near-IR) imaging and spectroscopic data to characterize its central star, the surrounding nebular emission, and its local ISM environment. By combining these observations with archival data at longer wavelengths, we aim to constrain the true nature of this source and to understand its role in the broader context of the star formation process in this region.

This manuscript is organized as follows. Section 2 outlines the observations and data processing. The results from imaging and ancillary maps are presented in Sect. 3. The near-IR spectroscopic analysis is presented in Sect. 4, where we analyze the central source and the nebular gas. In Sect. 5, we derive the distance to IRAS 16475–4609 and evaluate the physical parameters of the H II region. Finally, the main conclusions are discussed in Sect. 6.

2. OBSERVATIONS AND DATA REDUCTION

2.1. NEWFIRM/CTIO

Near-IR narrow and broad-band imaging observations were carried out using the wide-field near-IR camera NEWFIRM ([Autry et al. 2003](#)) installed on the 4-m Victor Blanco telescope at CTIO (Cerro Tololo, Chile) on July 18th, 2024. NEWFIRM has a detector mosaic of four $2\text{k}\times2\text{k}$ InSb arrays, providing a FOV of $27'.6\times27'.6$ with a cross-shaped $35''$ -wide gap between the arrays.

Observations were performed using the narrow-band Fe II ($1.644\ \mu\text{m}$), H₂ ($2.144\ \mu\text{m}$) and Br γ ($2.168\ \mu\text{m}$), and the broad-band H and K filters. A four-point dithering pattern spaced by $82''$ in a 2×2 grid was adopted to suppress defects on the detector. The NEWFIRM observations are summarized in Table 1.

Basic data reduction (flat-field correction and sky subtraction) was performed using the IRAF MSCRED package. The astrometric solution and distortion correction of the field were obtained by comparing the field with reference stars in the 2MASS catalog using SExtractor and Scamp ([Bertin et al. 2002](#)), leading to positional errors smaller than $0''.10$. Finally, the individ-

ual images were median-combined using **Swarp** (Bertin et al. 2002).

The continuum subtraction of the narrow-band images was performed by scaling the broad-band image with a fixed factor, determined by minimizing the residuals of point sources across the FOV. This multiplicative factor was derived through an iterative process, adjusting the scale until the stellar residuals in the resulting narrow-band frame were minimized, ensuring that the scaled continuum contribution from the broad-band image was then subtracted from the narrow-band frame to isolate the emission-line features.

Table 1. Log of NEWFIRM/CTIO observations.

Filter	$\lambda/\Delta\lambda$ (nm)	MJD	t_{exp} (sec)	Airmass	FWHM (")
Fe II	1649.1/17.2	60479.235	16×60	1.12	1.170±0.055
H ₂	2131.9/24.0	60479.242	16×60	1.13	1.188±0.061
Br γ	2177.0/24.4	60479.253	17×60	1.16	1.164±0.049
H	1631/308	60479.273	12×2	1.23	1.174±0.086
K	2150/320	60479.267	13×2	1.20	1.090±0.041

2.2. Broad-band near-IR images from VVV

We obtained ancillary near-IR images in the broad-band *JHK_s* filters taken with the VISTA telescope and part of the VISTA Variables in the Via Lactea (VVV) survey (Minniti et al. 2010). The images have a plate scale of 0.34" pixel⁻¹ and median FWHM of 1.07±0.07".

2.3. TripleSpec4.1/SOAR

Spectroscopic observations were carried out with the TripleSpec 4.1 near-IR Imaging Spectrograph (TripleSpec, Schlawin et al. 2014) at the Southern Astrophysical Research Telescope (SOAR, Cerro Pachón, Chile). TripleSpec is a cross-dispersed spectrograph with a fixed 1.1×28" slit, providing a full spectral coverage from 0.94 to 2.47 μm (R~3,500), encompassing the entire *YJHK* photometric range.

Observations were carried in 2022 July 30th, with airmass of 1.92. We adopted an AABAA dither pattern with an exposure time of 150 sec per frame, where A and B correspond to a on- and off-source positions, respectively. The B position was set to a nearby nebular-free position. In order to map both the point source and the extended nebulosity, we adopted a position angle of 50°, as indicated in Fig. 2.

2.4. Spectroscopic Data Reduction

The TripleSpec/SOAR data was processed using a modified version of the IDL-based **Spextool** pipeline

Cushing et al. (2004), for use at SOAR. The data reduction steps include flat-field correction, wavelength calibration using a CuHeAr arc lamp, removal of emission sky features by subtracting A and B exposures, and extraction of the one-dimensional spectra. We used observations of the telluric standard star HIP 82091 observed at similar airmass values (1.84) to perform the telluric correction and flux calibration of the spectrum. The final one-dimensional near-IR spectrum has a peak SNR of ~300 at the center of the K-band.

2.4.1. Two-dimensional TripleSpec/SOAR spectroimages

Spectroimages of orders $n = 3$ to 7 were obtained using the IDL **tspec_spectro2d**¹ procedure as described below.

Input raw data of on- (*ON*) and off-source (*OFF*) positions are divided by the flat-calibration frame created by **Spextool**. Then, the images are subtracted (producing a *ON_{sub}* frame), so the discrete telluric emission lines are suppressed from the on-source exposure. The user can improve the sky subtraction by modifying the multiplicative **off_ratio** parameter (default value equals to one), defined as:

$$ON_{\text{sub}} = ON - OFF \cdot \text{off_ratio}$$

The wavelength and spatial solutions obtained by **Spextool** were used to retificate the data in a linear grid for both spectral and spatial dimensions, by keeping the original plate scale (0.3376" pixel⁻¹) and spectral dispersion of the instrument for each order.

Finally, the one-dimensional flux calibration solution obtained by the **xtelcorr** procedure was used to convert flux from DN s⁻¹ to W m⁻² μm^{-1} units.

Final two-dimensional images of the four on-source exposures were median-combined, suppressing noise and cosmic rays. Figure 1 exhibits the spectroimage of order $n = 3$ (*K*-band) as an example.

3. THE STRUCTURE OF IRAS 16475-4609

In this section, we analyze the structural characteristics of IRAS 16475–4609 through near-infrared imaging, focusing on the interplay between the central source and its surrounding nebulosity. Figure 2 presents the near-IR maps obtained in both broad- and narrow-band filters. The false color *JHK_s* map (central panel) reveals a nebulosity extending northeast (NE) from the bright source at the center of the FOV. The nebular emission exhibits a conical shape, suggesting that the

¹ the IDL and Python versions of **tspec_spectro2d** routine can be found at <https://github.com/navarete/>

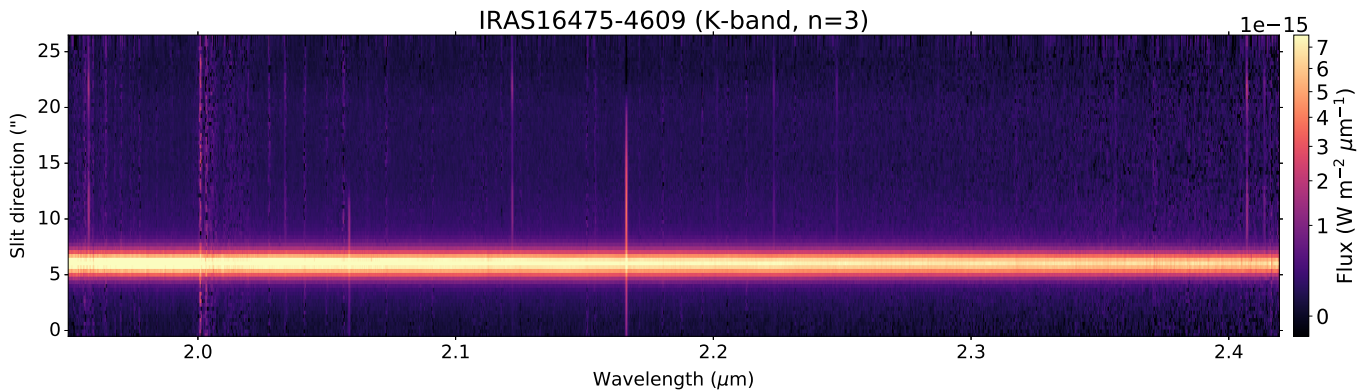


Figure 1. Two-dimensional spectroimage of the order $n=3$ (K-band) resampled into a 2040×80 pixel linear grid.

ionizing source has carved a cavity within a dense molecular cloud. Such interpretation is supported by the presence of deeply embedded near-infrared objects located to the south (S) and west (W) of the source, likely hidden within the dusty environment.

The K -band emission (top left panel) indicates that the continuum emission extends radially up to $\sim 24''$ from the central source, predominantly in the NE direction. In general, the K -band nebosity is often associated with dust that has been heated by a nearby hot source.

The remaining panels in Fig. 2 present continuum-subtracted narrow-band maps, exhibiting the emission of molecular hydrogen at $2.12 \mu\text{m}$ (H_2 , lower left), the forbidden Fe II line at $1.664 \mu\text{m}$ (top right), and the $\text{Br}\gamma$ transition at $2.166 \mu\text{m}$ (lower right). The $\text{Br}\gamma$ and Fe II maps probe the ionized gas in closer proximity to the central source. Notably, the unobstructed view to the NE direction displays a spherical morphology, characteristic of the ionization front typically generated by a massive star. In contrast, the H_2 emission traces the outer layer of the continuum nebosity and the compact ionized gas, suggesting its location along the conical surface on the molecular cloud.

The hypothesis of a high column density dusty region to the W direction of the central source can be further investigated at longer wavelengths. This region of the sky is covered by the sub-millimeter (sub-mm) observations from the APEX Telescope Large Area Survey of the Galaxy (ATLASGAL, Schuller et al. 2009). ATLASGAL provides a high-sensitivity view of the inner Galaxy at $870 \mu\text{m}$, with an angular resolution of $19''$, enabling the study of regions associated with dense cold gas and dust, particularly in star-forming regions. Figure 3 presents the near-infrared JHK_s map overlaid with the $870 \mu\text{m}$ contours (white curves). The sub-mm emission traces an elongated structure peaking at $\sim 130''$ to the W direction of the bright near-IR source within IRAS 16475–4609. The near-IR source is at the

same position as the ATLASGAL source identified as G339.7187–1.2041 (Csengeri et al. 2014). This entire sub-mm structure has a projected length of about $150''$ and is located near a compact, bright sub-mm structure situated to the S direction, lying outside of the FOV of the map presented in Fig. 3. Notably, the bright point-like source position lies at the edge of this extended sub-mm structure, which accounts for the inhomogeneous morphology of the K -band continuum emission extending toward the NE direction.

We further compared the near-IR and sub-mm maps with Australia Telescope Compact Array (ATCA) radio observations at 8.6 GHz (3 cm, beam size of $2''.11 \times 1''.21$, red lines) and 4.8 GHz (6 cm, $3''.08 \times 1''.76$, black lines), presented by Urquhart et al. (2007). These observations are indicated as the red (3 cm) and black contours (6 cm) in Fig. 3. As typically observed in compact H II regions, the centimeter emission traces a compact region coinciding with the peak intensity of the near-IR emission. The 3-cm emission is more extended than the 6-cm emission, with both structures oriented toward the east of the source.

The centimeter emission exhibits a cometary morphology, consistent with the classification of UCH II regions proposed by Wood & Churchwell (1989a), indicating a parabolic ionization front. This particular morphology is often attributed to the supersonic motion of the ionization front through the surrounding neutral gas. However, the $\text{Br}\gamma$ contours (blue curves) reveal that the ionized front encompasses a much larger area than the centimeter emission, which primarily probes the peak intensity of the ionized gas surrounding the central star.

4. THE NEAR-INFRARED SPECTROSCOPIC ANALYSIS OF IRAS 16475–4609

In this section, we present the spatially integrated analysis of the near-IR spectrum of the central source powering the H II region and the associated nebosity towards IRAS 16475–4609. The one-dimensional nor-

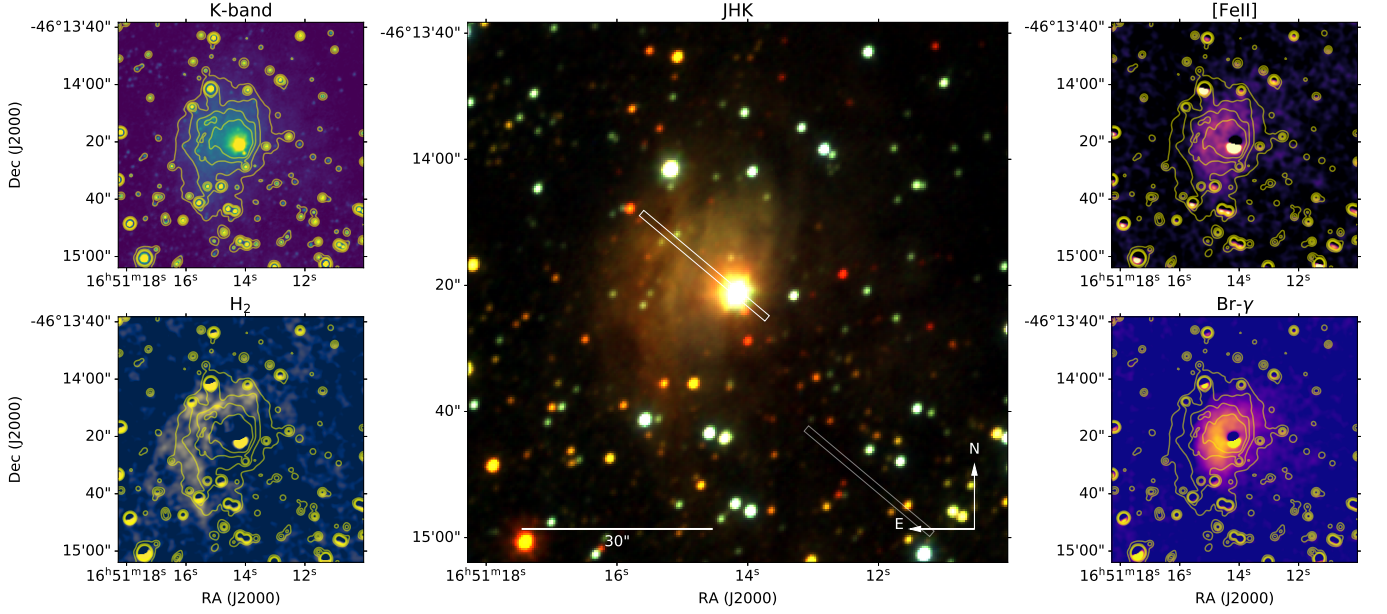


Figure 2. NEWFIRM/CTIO and VVV/VISTA observations of IRAS 16475–4609. The central panel shows a false-color RGB map from VVV (blue: J, green: H, red: K_s) of a $85 \times 85''$ region centered at RA = 16:51:14.156, Decl. = $-46:14:21.23$ (J2000). The white and grey rectangles indicate the A and B positions for the TripleSpec observations. A $30''$ scale bar is indicated in the lower left region of the panel. The top left panel shows the NEWFIRM K-band image of the same FOV, overlaid by contours highlighting the continuum emission at 15, 30, 45, and 60% of the nebulosity peak intensity. The other panels show the continuum-subtracted H_2 map ($2.12 \mu\text{m}$, lower left), Fe II ($1.644 \mu\text{m}$, upper right), and Br γ ($2.166 \mu\text{m}$, lower right), overlaid by the K-band contours.

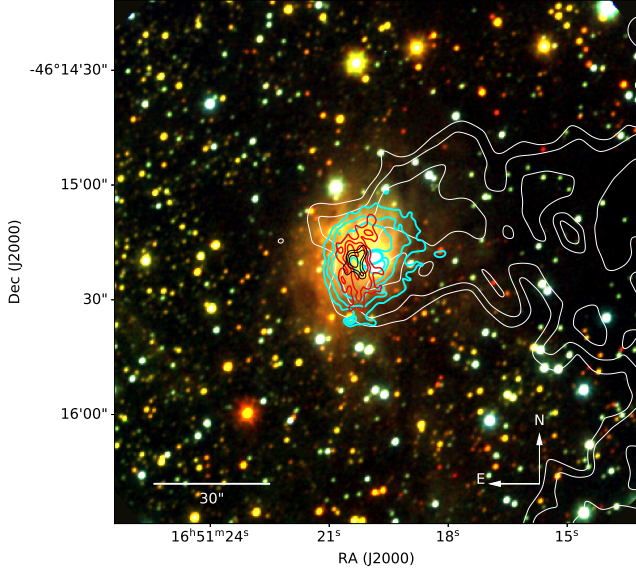


Figure 3. VVV/VISTA observations of IRAS 16475–4609 in a 2.25×2.25 region. The map shows a false-color RGB image highlighting the nebular emission around the IRAS object. A $30''$ scale bar is indicated in the lower left region of the panel. The contours indicate the emission at $870 \mu\text{m}$ from ATLASGAL (white curves), the ATCA maps at 3 cm (red) and 6 cm (black), and the near-IR Br γ emission (cyan).

malized spectrum of the point source and the extended nebular emission (scaled by a 0.05 factor) are presented

in Fig. 4. Strong nebular emission lines, such as Br γ and He I at $2.0587 \mu\text{m}$, have been suppressed to highlight the weaker lines.

The point source spectrum (black curve) exhibits relatively broad photospheric H I recombination lines in absorption, typical features observed in main sequence stars. A narrow H I emission component is superimposed on these photospheric absorption features, likely arising from the surrounding nebulosity detected in the near-infrared images (Fig. 2). The near-infrared spectrum was used to classify the spectral type of the central source in Sect. 4.1.

The nebular spectrum (blue curve) exhibits a typical spectrum of an H II region, with the H I features observed as narrow emission lines. Additional emission features include He I at 1.083 and $2.058 \mu\text{m}$, a strong forbidden [S III] line at $0.9534 \mu\text{m}$, and at least four [Fe II] features between 1.25 and $1.65 \mu\text{m}$. Several molecular hydrogen (H_2) lines are also identified in the nebular spectrum. Fainter unmarked emission features, particularly toward longer wavelengths, correspond to residual telluric emission lines that were not fully removed from the data. The nebular spectrum is further analyzed in Sect. 4.2, with a detailed analysis of the H_2 emission in Sect. 4.2.1.

4.1. Characterization of the central source

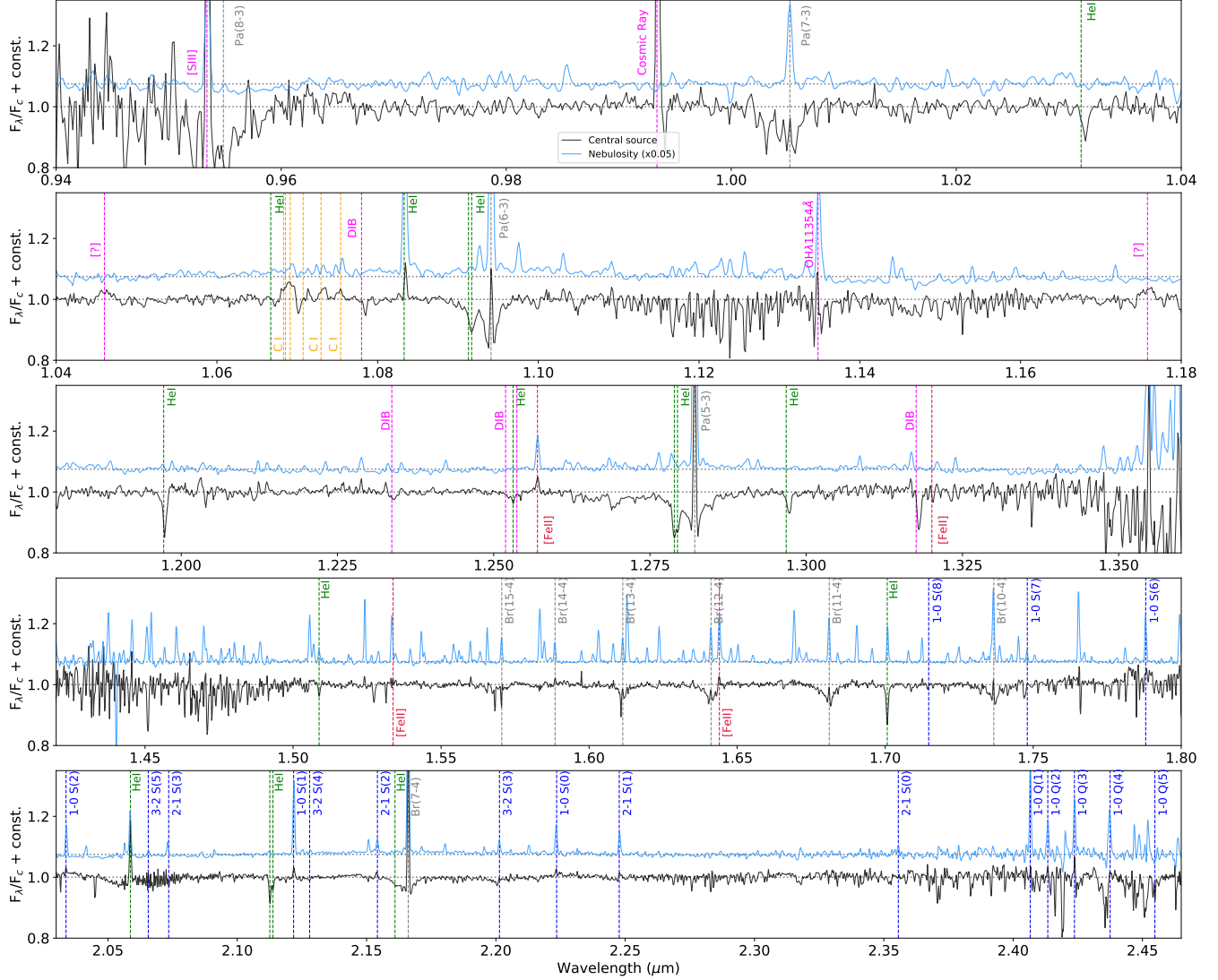


Figure 4. Continuum-normalized near-IR spectrum of IRAS 16475 (black curve) and the associated nebulosity (blue). The nebular spectrum was scaled by a factor of 0.05 with respect to the central source. Vertical dashed lines indicate the wavelength of relevant spectral features: H I (gray lines) and He I (blue), Fe II (red), C I (yellow), [S II], DIB and some unknown transitions (magenta).

Fig. 4 presents the normalized spectrum of the central source towards IRAS 16475–4609. We will discuss the identified spectral features across the full wavelength range covered by our observations, with an emphasis on the H- and K-band windows, which are crucial for spectral classification based on the scheme from [Hanson et al. \(1996, 2005\)](#). The equivalent widths of the key spectral lines are summarized in Table 2.

Due to the non-uniform distribution of the nebular emission along the slit (see Figs. 7 and 8), the H I features exhibit complex profiles. Notably, the Pa β line at 1.28 μ m and Br γ at 2.1661 μ m exhibit a combination of narrow nebular emission superimposed on broad absorption features.

We detect the Pa γ and Pa δ transitions at 1.094 and 1.005 μ m, respectively, though Pa δ is blended with a strong, narrow [S III] emission feature at 0.9532 μ m, which appears on its blue wing.

The H-band exhibits the higher-order Brackett series transitions up to (15-4) at 1.5705 μ m. Higher transitions are not detected likely due to the limited signal-to-noise ratio (SNR) of the data. Similar to Br γ , these Brackett lines also exhibit narrow emission components superimposed on the broad absorption feature, indicating the complex surrounding nebular environment.

Nebular emission is likely associated with two He I features: $2^3\text{P}-2^3\text{S}$ at 1.083 and $2^1\text{P}-2^1\text{S}$ 2.058 μ m; while several other He I transitions are detected only in ab-

sorption. The strongest He I absorption features correspond to the $5^3D - 3^3P$ transition at $1.1973 \mu\text{m}$, the $4^3P - 3^3P$ at $1.70 \mu\text{m}$ and the $4^3S - 3^3P/4^1S - 3^1P$ doublet at $2.11 \mu\text{m}$ with no clear emission counterpart.

A few relatively weak J-band emission features were detected, in particular the C I multiplet at 10686\AA , including the $^3P_2^0 - ^3D^1$ feature at 10675\AA , absent in the spectral atlas from (Groh et al. 2007, see their Table 2). Two relatively weak and broad emission features with no clear identification are labeled at the following wavelengths: 10460\AA and 111758\AA . The bright peak at 9934\AA is identified as a cosmic ray residual, and a strong residual peak at 111348\AA is attributed to poor sky subtraction within the H_2O telluric band between $1.11\text{--}1.16 \mu\text{m}$. A few diffuse interstellar band (DIBs) candidates were identified at 1.234 , 1.253 , 1.297 and $1.318 \mu\text{m}$, consistent with those reported by Hamano et al. (2022).

4.1.1. Spectral Type Classification

The normalized K-band spectrum of IRAS 16475–4609 reveals no clear detection of spectral features typically associated with early- and mid-O type stars, such as the C IV triplet, the N III emission, or He II absorption. The absence of N III emission implies a spectral type no earlier than O9 V, while the strong He I absorption at $2.11 \mu\text{m}$ suggests a spectral type earlier than B5 V. Given the absence of ionized He II lines, the spectral type classification scheme for late-O and early-B stars relies on the relative strengths of H I and He I features, which are less sensitive to stellar parameters than those of early to mid O-type stars (Hanson et al. 1996, 2005).

A visual comparison between the spectrum of IRAS 16475–4609 and the OB atlases from Hanson et al. (1996, 2005) suggests a spectral type ranging from O9.5 V (e.g., HD 37468, which exhibits relatively weaker H I lines compared to those observed in Fig. 4) to B2 V (e.g., HD 36166, which shows weaker He I absorption at $2.11 \mu\text{m}$).

To further refine the spectral type classification, we took advantage of a complementary atlas of OB stars observed with TripleSpec (Navarete et al., in prep.), which extends the spectral coverage of the OB star atlases from Hanson et al. (1996, 2005) to a broader wavelength range of $0.94\text{--}2.47 \mu\text{m}$, providing data with relatively high signal-to-noise ratios (SNR). The TripleSpec atlas encompasses luminosity class V stars from early O to early A-type, including all equatorial and southern targets from Hanson et al. (1996, 2005), along with additional well-known OBA stars observable from the SOAR telescope (Decl. $< 30^\circ$). This expanded coverage allows for a more precise comparison across a wider

Table 2. Equivalent width measurements for H I, He I, and DIB features identified in the stellar spectrum of IRAS 16475–4609.

Line	Transition	λ_0 (\AA)	λ_{obs} (\AA)	EW (\AA)
He I	$6^3S - 3^3P$	10667	10672.61	0.1797
He I	$2^3P - 2^3S$	10830	10834.77	-0.3835
He I	$5^3D - 3^3P$	11970	11973.21	1.1815
He I	$5^3F - 3^3D$	12789	12791.07	1.0679
He I	$5^1D - 3^1P$	12986	12972.56	0.4377
He I	$4^1P - 3^1S$	15084	15089.06	0.4331
He I	$4^3P - 3^3P$	17002	17006.99	1.2192
He I	$2^1P - 2^1S$	20580	20586.88	-1.2158
He I	$4^3S - 3^3P$	21126	21129.98	1.0957
H I	Br(15)	15705	15686.82	1.5483
H I	Br(14)	15885	15822.56	0.4522
H I	Br(13)	16114	16111.53	1.0125
H I	Br(12)	16412	16407.19	1.9932
H I	Br(11)	16811	16807.89	2.8048
H I	Br(10)	17367	17366.25	1.5490
H I	Br(8)	19451	19450.30	3.5946
H I	Br(7)	21661	21657.67	-0.0237
H I	Pa(7)	10052	10044.89	3.4552
H I	Pa(6)	10941	10933.87	3.1441
H I	Pa(5)	12822	12814.82	2.2834
DIB		10280	1280.90	0.1582
DIB		12337	12339.82	0.3285
DIB		12692	12692.49	0.5933
DIB		13180	13180.92	0.9562
DIB		15273	15273.68	0.5283
DIB		15653	15654.00	0.2438
DIB		16573	16575.12	0.0551

Notes: The columns are as follows: (a) Atom, (b) transition, (c) Rest wavelength, (d) Observed wavelength, (e) equivalent width.

spectral range, matching the same spectral resolution of IRAS 16475–4609 observations ($R \sim 3500$).

In Fig. 11 (Appendix A), we present four key spectral regions that highlight the primary features used for the spectral type classification of IRAS 16475–4609, comparing its normalized spectrum with six OB standards spanning the O9.5–B2 V range. A more detailed analysis of the H I features narrows the spectral type of the central source to the O9.5–B0.7 V range, refining the broader classification initially derived from visual inspection of the OB star atlases by Hanson et al. (1996, 2005).

We further compared the emission-free He I line profiles from the IRAS 16475–4609 spectrum with those of

the OB standards observed with TripleSpec to check if the spectral type classification could be improved. Figure 5 presents eight spectral windows containing He I lines that serve this purpose. In general, most of the He I absorption features match the profiles observed in B0 and B0.7 V stars, including the He I absorption at $1.297 \mu\text{m}$, which is strongly affected by the blue wing of the $\text{Pa}\beta$ line. In addition, the strength of the C I multiplet around 10686 \AA further supports a classification of the central source as an early-B star, no later than B0.7 V.

4.2. Analysis of the extended nebular emission

We took advantage of the spatial information provided by the TripleSpec spectroscopic observations to further investigate the extended emission detected in the narrow-band images of IRAS 16475–4609 (Fig. 2).

Spectroimages, which display spectral dispersion along the slit direction, were extracted for selected emission lines using the IDL `tspec_extract_lines` procedure (see Sect. 2.4.1). This method applies an outlier-resistant polynomial fit to model the continuum, which is then subtracted from the data. The emission lines are modeled with Gaussian profiles using the `MPFITPEAK` routine.

The total flux ($\Sigma F_\lambda d\lambda$, in W cm^{-2} units) is integrated within a 90% confidence interval based on the fitted model. Figure 6 illustrates the result for the H_2 (1–0) S(1) transition at $2.1218 \mu\text{m}$.

Figure 7 presents the continuum-subtracted spectroimages for the He I ($\lambda = 2.0578 \mu\text{m}$), the H_2 (1–0) S(1) ($\lambda = 2.1218 \mu\text{m}$), and the $\text{Br}\gamma$ ($\lambda = 2.1661 \mu\text{m}$) features. The spatial axis (y-axis) reveals distinct morphologies for each transition, suggesting that they trace different phases of the extended emission associated with IRAS 16475–4609. No significant clear velocity gradient is observed along the spectral direction (x-axis) for any of these features.

To better visualize the flux distribution along the slit, Fig. 8 shows the integrated flux of each spectral line as a function of the slit position, alongside the K-band continuum emission (black curve).

The continuum emission peaks sharply at the position of the central source, indicating a minimal contribution from extended continuum emission. The $\text{Br}\gamma$ emission (green curve) traces extended ionized gas, peaking $\approx 5''$ from the central source, and gradually decreases out to $\sim 16''$. This distribution is consistent with a wide-angle conical outflow of ionized gas, with the flux increasing with distance from the star due to the expanding ionization front, reaching a maximum where ionization is most

efficient, and then decreasing as fewer neutral atoms can still be excited by the UV radiation from the central star.

The He I emission (in red) exhibits a similar, though more compact, spatial profile, extending to $\sim 6''$ from the central star and peaking closer, at $\sim 3''$. This suggests that the He excitation radius is smaller than that of H, consistent with the fact that He requires higher energies to be excited.

The molecular hydrogen line (in blue) displays a double-peak profile, with emission maxima at $\sim 5''$ and $\sim 16''$ from the central source. The inner peak coincides with the outer boundary of the He I distribution and the peak of the $\text{Br}\gamma$ emission, while the outer peak encircles the H II region in a shell-like structure, likely tracing the photodissociation region (PDR). Between these peaks, the H_2 emission persists at a lower level, suggesting a gradual transition zone where the molecular gas is partially shielded from direct stellar radiation, but still influenced by the expanding ionization front. This non-zero emission could indicate a clumpy or filamentary distribution of molecular material, allowing for survival even within regions closer to the ionization boundary.

4.2.1. Molecular H_2 analysis

We constructed spectroimages for selected H_2 lines to extract their integrated flux. Table 3 lists the fluxes and the physical properties of K-band H_2 transitions detected above the $1\text{-}\sigma$ level. The integrated fluxes were obtained from the corresponding spectroimages for each transition (e.g., Fig. 7). Using the continuum-subtracted fluxes of the individual H_2 lines, we constructed a ro-vibrational Boltzmann diagram of the H_2 molecule to derive the physical parameters of the molecular gas, assuming local thermodynamic equilibrium (LTE).

Assuming a Boltzmann distribution and optically thin emission, the observed H_2 fluxes F_J follow the relation:

$$\frac{4\pi F_J}{\Omega h \nu_J g_J A_J} = \frac{N_J}{g_J} = \frac{N_{\text{tot}}}{Q_{\text{rot}}} \exp(-E_J/k_B T_{\text{exc}}) \quad (1)$$

where h is the Planck constant, k_B is the Boltzmann constant (in erg K^{-1}), Ω is the emitting area solid angle (in sr), ν_J is the frequency (in Hz), g_J is the statistical weight, A_J is the Einstein coefficient (in s^{-1}), N_J is the upper-level column density of the H_2 transition (in cm^{-2}), N_{tot} is the total column density of the H_2 molecule (in cm^{-2}), Q_{rot} is the partition function, E_J is the upper-level transition energy (in erg), and T_{rot} is the rotational temperature (in K).

The total column density and temperature of the gas are estimated through the linear fit defined as:

$$\ln\left(\frac{N_J}{g_J}\right) = \ln\left(\frac{N_{\text{tot}}}{Q_{\text{rot}}}\right) - \frac{E_J}{k_B T_{\text{rot}}} = \beta + \alpha E_J \quad (2)$$

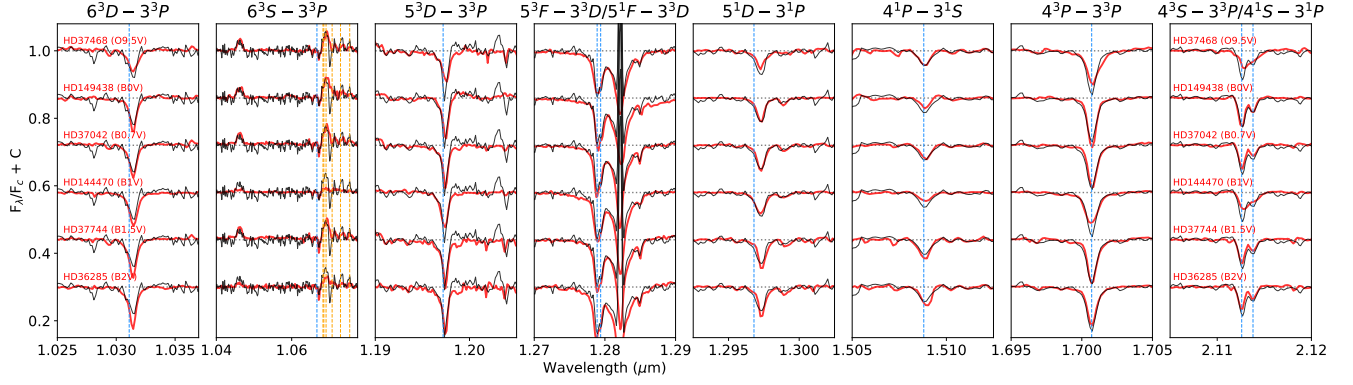


Figure 5. Zoom around He I lines in the continuum-normalized near-IR spectrum of IRAS 16475–4609. The red curves are a sample of representative OB-type stars observed with TripleSpec (Navarete *et al.*, in prep.), from top to bottom: HD37468(O9.5 V), HD149438 (B0 V), HD37042 (B0.7 V), HD144470 (B1 V), HD37744 (B1.5 V), and HD36285 (B2 V). The vertical dashed lines indicate He I (blue), and C I (yellow) lines used for classification.

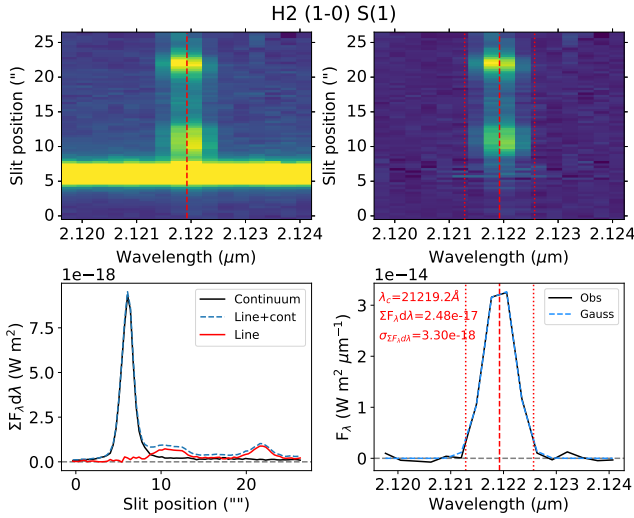


Figure 6. Spectro image of the H₂ (1-0) S(1) transition at 2.1218 μm towards IRAS 16475–4609. Top panels: Spectroimages of the total flux (line+continuum, left) and the continuum-subtracted emission (right). The vertical dashed red line marks the center of the profile, while the vertical dotted red lines indicate the spectral range used to integrate the total flux. Bottom left: Spatial distribution along the slit for the (a) total flux (line+continuum, dashed blue curve), (b) continuum-subtracted line emission (solid red curve), and (c) continuum emission (solid black). Bottom right: Continuum-subtracted integrated spectrum. The vertical lines are the same as defined in the top right panel. The Gaussian fit to the emission line is shown by the dashed blue curve. The central wavelength, the integrated flux and its error are indicated in the top left corner.

Eqs. (1) and (2) require reddening-corrected fluxes and the latter can also be used to infer the K-band extinction (A_{Ks}). By following the procedure outlined by Caratti o Garatti *et al.* (2015), one can vary A_{Ks} to identify the value that maximizes the correlation be-

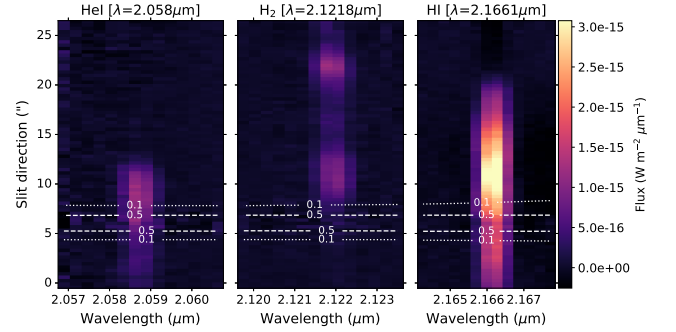


Figure 7. Spectroimages of the He I ($\lambda = 2.0587 \mu\text{m}$, left panel), H₂ (1-0) S(1) ($\lambda = 2.1218 \mu\text{m}$, middle) and Br γ ($\lambda = 2.1661 \mu\text{m}$, right). The color bar to the right indicates the flux intensity for all three features. White contours represent the continuum emission, with the dashed and the solid lines at 10 and 50% of the peak intensity, respectively, marking the position of the point-like source.

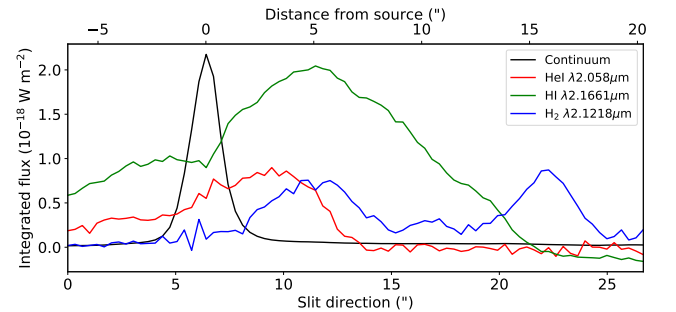


Figure 8. Integrated flux of the extended emission along the slit. The Br γ , H₂, and He I emission from Fig. 7 are represented by the green, blue, and red curves, respectively. The black curve indicates the position of the point-like source. The top x-axis shows the slit direction in arcsecond units centered on the location of the point-like source.

tween $\ln\left(\frac{N_L}{g_J}\right)$ and E_J . The top panel of Fig. 9 shows

Table 3. K-band H_2 fluxes extracted from spectroimages from the near-IR spectroscopic observations towards IRAS 16475–4609.

Transition	Flux ($10^{-18} \text{ W m}^{-2}$)	σ_F (μm)	λ (μm)	g	E_{upper} (K)	A (10^{-7} s^{-1})
2-1 S(5)	9.24	0.91	1.9449	45	15763	5.05
1-0 S(3)	32.30	0.96	1.9576	33	8365	4.21
1-0 S(2)	11.00	1.02	2.0338	9	7584	3.98
3-2 S(5)	1.94	0.97	2.0656	45	20856	4.50
1-0 S(1)	24.20	0.94	2.1218	21	6956	3.47
3-2 S(4)	1.18	0.93	2.1280	13	19912	5.22
2-1 S(2)	6.22	1.01	2.1542	9	13150	5.60
3-2 S(3)	2.59	0.85	2.2014	33	19086	5.63
1-0 S(0)	10.10	0.96	2.2235	5	6471	2.53
2-1 S(1)	7.67	0.92	2.2477	21	12550	4.98
3-2 S(2)	2.08	0.87	2.2870	9	18386	5.63
3-2 S(1)	3.91	0.93	2.3864	21	17818	5.14
1-0 Q(1)	36.30	0.75	2.4066	9	6149	4.29
1-0 Q(2)	12.20	0.70	2.4134	5	6471	3.03
1-0 Q(3)	25.00	0.69	2.4237	21	6956	2.78
1-0 Q(4)	6.58	0.84	2.4375	9	7586	2.65

Notes: the energy levels are from [Dabrowski \(1984\)](#), and the Einstein coefficients are from [Turner et al. \(1977\)](#).

the Pearson correlation coefficient as a function of the K -band reddening, indicating that the strongest correlation occurs for $A_{K_s} = 1.80 \pm 0.1$ mag (corresponding to $A_V = 26.9 \pm 1.5$ mag assuming the A_V/A_K ratio of 14.95 from [Damineli et al. 2016](#)).

The bottom panel of Fig. 9 presents the Boltzmann diagram of the H_2 emission, corrected for extinction. The best fit line yields a slope of $\alpha = -0.257 \pm 0.018$, corresponding to a T_{rot} value of $(3.89 \pm 0.27) \times 10^3$ K. The linear coefficient corresponds to a total H_2 column density of $\log_{10}(N_{\text{tot}}/\text{cm}^{-2}) = 17.8 \pm 0.2$ dex.

Figure 10 presents the spatial distribution of the H_2 emission along the slit. The black curve represents the mean flux of the transitions listed in Table 3. The spatial profile reveals three distinct emission knots, labeled as A, B and C. Taking advantage of the spatial information in the spectroscopic data and fixing the A_{K_s} value at 1.80 mag, we evaluated the T_{rot} of the gas for each spatial pixel (spaxel) associated with the identified H_2 knots. A weighted mean T_{rot} value was then calculated for each knot (represented by the larger circles with error bars in the plot). Knot B, the weaker of the three, shows a slightly higher rotational temperature of $T_{\text{rot}} = (3.91 \pm 0.21) \times 10^3$ K when compared to the brighter knots A and C ($T_{\text{rot}} \sim 3 \times 10^3$ K).

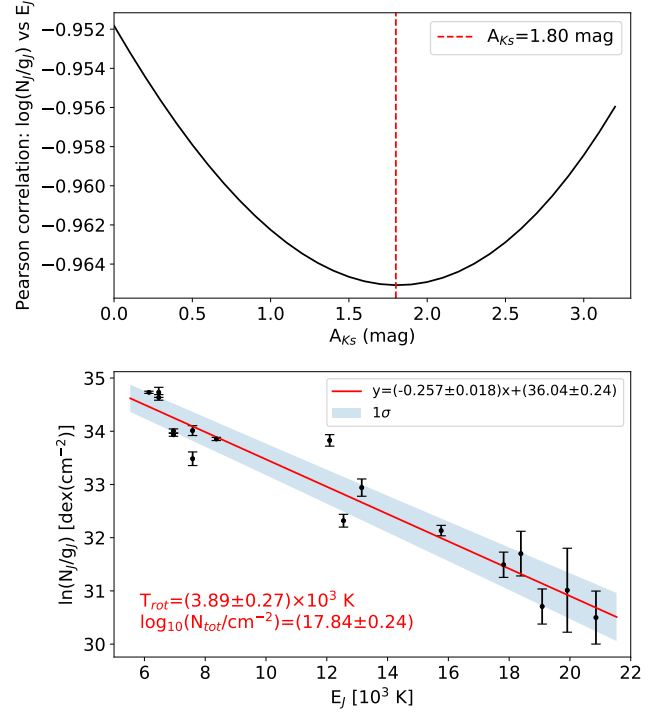


Figure 9. Analysis of the molecular hydrogen emission associated with the nebular component of IRAS 16475–4609. Top panel: Pearson correlation between the logarithm of the upper-level column density as a function of the upper-level energy of the H_2 transitions by varying the A_{K_s} values from 0 to 3.3 mag in steps of 0.1 mag. The best A_{K_s} value is indicated by the vertical dashed red line, corresponding to the value that maximizes the correlation. Bottom panel: Boltzmann diagram of the H_2 emission after correcting for reddening effects. The solid red line indicates the best fit to the data (values in the legend), and the shaded area shows the 1σ region of the fit. The corresponding T_{rot} and N_{tot} values from the best fit are indicated as red text.

The line ratios of H_2 transitions are powerful diagnostics in differentiating between excitation in shocks and PDRs formed by UV photons. For instance, the origin of the H_2 emission can be inferred using the ratio of H_2 transitions such as (1–0) S(1)/(2–1) S(1). From the fluxes listed in Table 3 we derived a (1–0) S(1)/(2–1) S(1) ratio of 3.6 ± 0.5 after correcting for reddening effects. As expected in a H II region, this ratio is closer to the predicted value of 1.8 for radiative excitation by UV photons from the protostar, rather than the theoretical value of ~ 10 expected for thermal excitation through shocks ([Black & Dalgarno 1976](#)). As indicated in Table 3, we do detect a few $v=3-2$ transitions, strongly suggesting that pure fluorescence may indeed occur, indicating excitation in a PDR rather than in shocks.

The bottom panel of Fig. 10 shows the integrated extinction-corrected fluxes for the two H_2 transitions (black: (1–0) S(1), orange: (2–1) S(1)) along the spatial

direction of the slit. The line ratio was calculated at each spaxel with fluxes above a $1\text{-}\sigma$ threshold for both transitions. The median ratio for each knot is indicated by the blue, black, and red points with associated error bars. The median ratios range from 3.5 to 5.0, consistent with the scenario of radiative excitation through UV photons, as expected for a H II region.

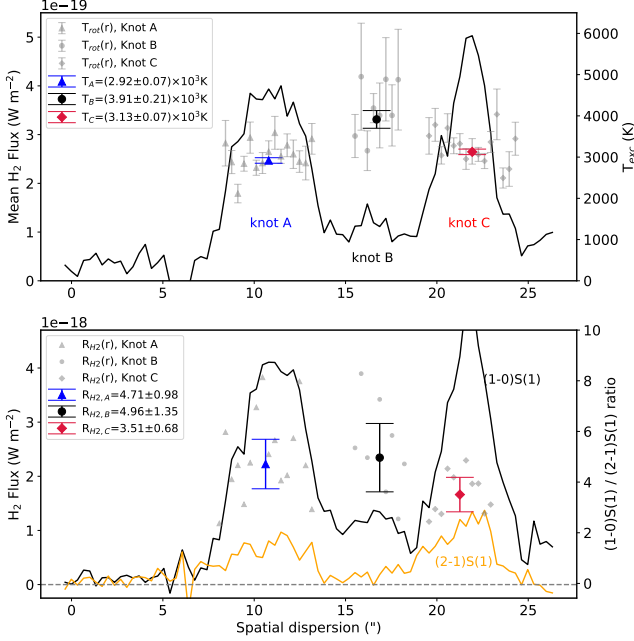


Figure 10. Top panel: Spatial distribution of the mean flux of 11 H₂ transitions along the slit direction (black curve). The gray points correspond to the T_{rot} of the gas evaluated at each spaxel. The colored points correspond to the weighted mean T_{rot} values for each of the three labeled H₂ knots: A (blue triangle), B (black circle) and C (red diamond). Bottom: Spatial distribution of the (1–0) S(1) and (2–1) S(1) transitions of the molecular hydrogen (blue and orange curves, respectively) corrected for extinction assuming $A_{K_s} = 1.80$ mag (Fig. 9), and the line ratio measurements (grey points). The colored points correspond to the weighted mean T_{rot} values for each of the three labeled H₂ knots: A (blue triangle), B (black circle), and C (red diamond).

5. DISTANCE AND IONIZING PHOTON BUDGET FROM IRAS 16475–4609

The accurate determination of the distance to IRAS 16475–4609 is crucial for understanding its physical properties and placing it within the broader context of star-forming regions and the Galaxy structure. In this section, we present three independent methods for deriving the distance to IRAS 16475–4609. First, we derive a spectrophotometric distance based on the spectral classification (Sect. 4.1) and near-IR photometry. Next, we present an independent distance estimate

based on the optical counterpart from Gaia Data Release 3. Finally, we use archival radio recombination line measurements to obtain the kinematic distance, providing a third, independent determination of the distance to IRAS 16475–4609.

With the distance to IRAS 16475–4609, we then evaluate the ionizing photon flux and the properties of the associated ionized gas.

5.1. The spectrophotometric distance to IRAS 16475–4609

The spectrophotometric distance to IRAS 16475–4609 was determined using the following approach. The visual absolute magnitude (M_V) for B0 and B0.5 V stars were obtained from Vacca et al. (1996), and their intrinsic V–K colors from Koornneef (1983). To ensure consistency with different photometric systems, we applied the transformations from Carpenter (2001) to convert the photometry to the 2MASS system.

Photometric data for IRAS 16475–4609 were extracted from the 2MASS catalog Skrutskie et al. (2006), yielding the following values: $m_{K_s} = 10.255 \pm 0.034$, $J-H = 0.925 \pm 0.040$, $J-K_s = 1.490 \pm 0.043$, $H-K_s = 0.565 \pm 0.045$ mag. To account for extinction, the K_s band extinction (A_{K_s}) was obtained by using the near-infrared color excess and applying Eqs. (15)–(17) from Damini et al. (2016). This method allowed us to correct for reddening effects and accurately derive the extinction-corrected magnitude, a critical step for determining the distance to the H II region.

The distance modulus ($\mu = m_{K_s} - M_{K_s} - A_{K_s}$) and the corresponding distance (d) for each Spectral Type are reported in Table 4, along with the relevant photometric properties. Given the uncertainty in the precise determination of the subspectral type, we computed the spectrophotometric distance for both B0 and B0.5 V subclasses individually, using their respective absolute magnitudes. We also computed the average distance by considering the mean absolute magnitude for the B0–B0.5 range. Based on this analysis, the mean distance to IRAS 16475–4609 is 3.6 ± 1.6 kpc.

Table 4. Photometric information and spectrophotometric distance determination towards IRAS 16475–4609.

Spectral Type	B0 V	B0.5 V	B0–B0.5 V
M_{K_s} (mag)	-3.31 ± 0.67	-3.26 ± 0.67	-3.28 ± 0.95
A_{K_s} (mag)	0.75 ± 0.07	0.74 ± 0.07	0.75 ± 0.10
μ (mag)	12.81 ± 0.67	12.77 ± 0.67	12.79 ± 0.95
d (kpc)	3.7 ± 1.2	3.6 ± 1.1	3.6 ± 1.6

5.2. Photogeometric distance from Gaia DR3

We searched for the optical counterpart of IRAS 16475–4609 using Gaia Data Release 3 (Gaia DR3; Gaia Collaboration et al. 2016, 2023), identifying two Gaia sources within $0''.84$ of each other. The brighter source, Gaia DR3 5940120644325949824, has a G -band magnitude of 16.6 with reliable astrometric and photometric measurements. The fainter source, Gaia DR3 594012064433998464 ($G = 17.7$ mag), has limited information in the Gaia archive and is detected only in the G -band. The results presented below consider only the brightest Gaia DR3 source with good photometric and astrometric measurements.

Table 5. Photometric and astrometric information of the Gaia DR3 counterpart associated with IRAS 16475–4609.

Gaia ID	5940120644325949824
G (mag)	16.6332 \pm 0.0039
BP-RP (mag)	3.756 \pm 0.030
A_G (mag)	5.94 $^{+0.38}_{-0.25}$
pmra (mas yr $^{-1}$)	−0.19 \pm 0.14
pmdec (mas yr $^{-1}$)	−2.25 \pm 0.11
parallax (mas)	0.22 \pm 0.12
RUWE	1.14
d_{geo} (kpc)	3.68 $^{+1.59}_{-1.07}$
$d_{photgeo}$ (kpc)	3.50 $^{+1.33}_{-0.89}$

The photogeometric distance reported for Gaia DR3 5940120644325949824 corresponds to $d_{GDR3} = 3.50^{+1.33}_{-0.89}$ kpc, with a re-normalised unit weight error (RUWE) below 1.4, (RUWE = 1.14), indicating a good astrometric solution (Lindgren et al. 2018). This distance corresponds to a distance modulus of $\mu_{GDR3} = 12.72^{+0.70}_{-0.72}$ mag, in close agreement with the spectrophotometric distance derived in Sect. 5.1.

5.3. Kinematic distance from Radio Recombination Lines

The *Southern H II Region Discovery Survey* (SHRDS, Wenger et al. 2021) reported a centimeter source (designated as SHRDS925, RA = 16:51:15.0, Dec. = −46:14:23.3) coincident with the near-IR source in IRAS 16475–4609. The radio source is associated with both continuum and hydrogen recombination line emission.

The hydrogen recombination lines (H88–H112) exhibit a mean peak velocity at $V_{lsr} = -33.2 \pm 0.2$ km s $^{-1}$ (Table 7 Wenger et al. 2021). We used the V_{lsr} information to evaluate the kinematic distance to IRAS 16475–4609,

using the Parallax-Based Distance Calculator² (Reid et al. 2016, 2019). To further constrain the distance estimate, we incorporated the proper motions of the Gaia DR3 counterpart (from Table 5). The uncertainties in both proper motion and V_{lsr} were propagated in the calculation, yielding a kinematic distance of 3.47 ± 1.26 kpc.

5.4. Ionizing Photon Budget and Spectral Type

With the distance to IRAS 16475–4609 established in the previous subsections, we now evaluate the ionizing photon flux and the properties of the associated ionized gas.

Under the assumption that the H II region is in photoionization equilibrium and optically thin, we estimated the Lyman continuum photon flux (N_{Ly} , in photons s $^{-1}$) using the integrated radio flux densities reported by Wenger et al. (2021, Table 5), and the modified version of Equation (7) from Carpenter et al. (1990):

$$\frac{N_{Ly}}{\text{photon s}^{-1}} = 7.7 \times 10^{43} \left(\frac{S_{int,\nu}}{\text{mJy}} \right) \left(\frac{d}{\text{kpc}} \right)^2 \left(\frac{\nu}{\text{GHz}} \right)^{0.1} \quad (3)$$

where $S_{int,\nu}$ is the integrated radio flux density at frequency ν (in mJy), d is the distance (3.51 ± 0.91 kpc, Table 6) and ν is the frequency of the observation (in GHz). We computed a Lyman continuum photon flux of $N_{Ly} = 47.36 \pm 0.06$ dex, based on a weighted mean of the individual SHRDS radio continuum measurements with frequencies ranging from 4.9 to 9.2 GHz.

We estimated the electron temperature (T_e , in K) using the radio recombination line (RRL) and the nearby continuum flux density measurements from SHRDS Wenger et al. (2021, Table 7), assuming optically thin emission in LTE (Shi et al. 2010):

$$\frac{T_e}{K} = \left[\left(\frac{6985}{\alpha(\nu, T_e)} \right) \left(\frac{\nu}{\text{GHz}} \right)^{1.1} \left(\frac{\Delta V_l}{\text{km s}^{-1}} \right)^{-1} \left(\frac{S_c}{S_l} \right) \left(1 + \frac{N(\text{He})}{N(\text{H})} \right)^{-1} \right]^{0.87} \quad (4)$$

where the dimensionless factor $\alpha(\nu, T_e)$ is the order of unity (Mezger & Henderson 1967), ΔV_l corresponds to the width of the line emission (in km s $^{-1}$), S_c/S_l is the ratio between the peak flux of the line and the nearby continuum, and $N(\text{He})/N(\text{H}) = 0.068 \pm 0.023$ (Wenger et al. 2013). Based on 19 RRL transitions (in the H88–H112 range) reported by Wenger et al. (2021), we derived a weighted mean electron temperature of $T_e = (5.44 \pm 0.21) \times 10^3$ K. This result is consistent for all the RRL transitions available from SHRDS, indicating robust physical conditions within the ionized gas.

² <http://bessel.vlbi-astrometry.org/>

6. DISCUSSION AND CONCLUSIONS

The multi-wavelength imaging analysis of IRAS 16475–4609 reveals a complex and dynamic environment around a massive star powering a young H II region at the edge of a molecular clump. This scenario is well aligned with the blister/champagne flow model described by Israel (1978) and later refined by Tenorio-Tagle (1979). In this model, an exciting star forms near the edge of a dense molecular cloud, causing ionization fronts to gradually advance into the cloud. This leads to the formation of a cavity filled with ionized gas, from which the gas flows away into space. Over time, a pressure gradient develops between the ionized gas and the neutral cloud, driving a shock that spreads the ionized material outward, creating an observable ionized nebula. Such a scenario aligns with the morphology observed in the IRAS 16475–4609 source, where the ionized region appears to expand into a conical cavity within the surrounding molecular material.

The near-infrared maps from Fig. 2 exhibit an extended nebulosity with a distinct conical morphology, suggesting a cavity created by the ionizing radiation of an early B-type star. This cavity is oriented towards the NE direction at the edge of a dense molecular clump, traced by the sub-mm 870 μm map from the ATLASGAL survey (see Fig. 3).

The narrow-band near-IR images reveal different phases of the nebulosity: Br γ and forbidden [Fe II] emission trace ionized gas with a spherical morphology close to the central source, while the H₂ transition at 2.12 μm highlights the excited molecular gas component at larger distances. As expected for a young H II region, the Br γ emission is compact and coincides with the position of the radio centimeter emission from ATCA, while the H₂ emission is more extended, originating in the surrounding molecular gas (Hanson et al. 2002).

This scenario is supported by Figs. 2 and 3, exhibiting the spatial distribution of these components. The H₂ emission probes the photodissociation region (PDR) at the interface between the ionized and neutral gas in the outer boundary of the extended *K*-band emission in IRAS 16475–4609. This pattern is consistent with UV-pumped molecular gas at the edges of a dense molecular clump, a characteristic structure often observed in young H II regions. The conical shape of the nebula to the northeast strongly suggests that the ionizing radiation has carved out an outflow cavity in this direction. The coupling between the Br γ and the compact centimeter emission indicates an evolving compact H II region. This configuration points to a scenario where the central ionizing source continues to interact with the surrounding dense molecular cloud. The compact ionized

core with extended molecular emission is a signature of UCH II regions that transition to more evolved phases as the ionized front gradually expands and disrupts the molecular cloud.

The H I recombination lines, on the other hand, trace the ionized gas closer to the central star. The extended Br γ emission observed in the *K*-band supports the presence of a dense, ionized region surrounding the central star, with the strongest emission concentrated in the northeast direction. This morphology is consistent with the hypothesis that the central star has cleared a cavity in the molecular cloud to the NE direction, allowing ionizing radiation to escape towards the interstellar medium.

The detection of deeply embedded near-infrared objects toward the southern and western directions of the *K*-band nebulosity suggests a region of high extinction to the west. Supporting this scenario, sub-mm emission from ATLASGAL reveals an elongated structure indicative of a high column density in that direction. Together, these observations provide a comprehensive view of the molecular cloud associated with IRAS 16475–4609, highlighting areas of dense gas and potential sites of triggered star formation as the ionization front advances into the quiescent molecular material.

6.1. Near-infrared characterization of the nebular emission in IRAS 16475–4609

The near-infrared TripleSpec/SOAR spectroscopic observations of the near-IR counterpart of IRAS 16475–4609 provided key insights into the characterization of the nebular emission and the nature of the central source powering the H II region in IRAS 16475–4609. By using by-products from the original Spextool IDL data reduction pipeline, we constructed spectroimages that enabled us to analyze the nebular emission associated with IRAS 16475–4609 along the slit of the TripleSpec/SOAR observations.

The analysis of the nebular emission revealed a typical H II region spectrum, characterized by narrow emission lines of H I and He I, alongside significant forbidden lines such as [S III] and multiple [Fe II] features. The roto-vibrational Boltzmann diagram of the H₂ emission was used to constrain the properties of the excited molecular gas, leading to a rotational temperature of $T_{\text{rot}} = (3.89 \pm 0.27) \times 10^3$ K and a column density of $\sim (6.3 \pm 3.0) \times 10^{17} \text{ cm}^{-2}$. By taking advantage of the spatial information of the spectroscopic data, we identified three H₂ knots (A, B, and C, Fig. 10) with distinct physical characteristics. Knot A is located closer to the central source powering the H II region, likely

tracing regions with higher excitation conditions due to its proximity to the ionizing star. In contrast, knot B is likely a low-density region, as indicated by its lower flux relative to knots A and C. This could occur due to a combination of factors, such as the local depletion of molecular gas caused by a stronger influence of stellar winds or radiation pressure from the central source, leading to a reduced emission in this region. The lower density of H_2 molecules may result in less efficient molecular hydrogen excitation, explaining the diminished H_2 emission towards knot B.

6.2. The massive star source powering the H II region in IRAS 16475–4609

Based on the OB classification scheme from [Hanson et al. \(1996, 2002\)](#), the presence of broad H I photospheric absorption features, along with He I absorption lines, suggests that the near-IR source is an early B-type massive star. Further comparisons with spectra from known OB standards observed with TripleSpec/SOAR refined the classification to a spectral type between B0 and B0.7 V (Sect. 4.1).

We provide three independent distance estimates for IRAS 16475–4609 using spectrophotometric, astrometric, and kinematic methods (Sect. 5). Using available 2MASS photometry (Sect. 5.1), we derived a spectrophotometric distance of 3.6 ± 1.6 kpc to the central source powering the H II region. For a single-object measurement, the uncertainty associated with the spectrophotometric distance is relatively larger ($\sim 44\%$) due to the error of the absolute visual magnitude calibration (± 0.67 mag) from [Vacca et al. \(1996\)](#). The scenario is even worse when adopting other works such as [Wegner \(2006\)](#), where uncertainties in the absolute magnitude exceed ± 2 mag. Future improvements in the fundamental parameters of OB stars can be achieved by combining data from recent all-sky surveys (e.g., Gaia DR3) with state-of-the-art photospheric models of massive stars (e.g., *Isosceles*; [Araya et al. 2023](#)).

Astrometric and photometric measurements from GaiaDR3 (Sect. 5.2) yield a photogeometric distance of $3.50^{+1.33}_{-0.89}$ kpc, which is consistent with the spectrophotometric distance and provides an independent confirmation of the distance to IRAS 16475–4609. Additionally, by leveraging the hydrogen recombination line measurements from SHRDS (Sect. 5.3), we determined a kinematic distance of 3.47 ± 1.26 kpc. This value is in agreement with both the spectrophotometric and Gaia-based estimates, further reinforcing the distance determination. All three distance estimates are listed in Table 6.

Combining these three distance estimates yields a weighted mean distance of 3.51 ± 0.74 kpc, correspond-

Table 6. Summary of the distance estimates to IRAS 16475–4609.

Distance (kpc)	Method
3.6 ± 1.6	Spectrophotometric (Sect. 5.1)
$3.50^{+1.33}_{-0.89}$	Parallax (Sect. 5.2)
3.47 ± 1.26	Kinematic (Sect. 5.3)
3.51 ± 0.74	Weighted mean distance

ing to a distance modulus of $\mu = 12.72^{+0.41}_{-0.51}$ mag. Considering that this is a single-object measurement, the resulting uncertainty of approximately 21% on the weighted mean distance is relatively small for such large distances. According to the Galactic structure models of [Reid et al. \(2019\)](#), such distance is broadly consistent with the expected locations of either the Scutum-Crux near arm (3.5 kpc) or the near side of the Norma arm (5.5 kpc). While spiral arm assignments remain uncertain due to variations in distance estimates and arm definitions, a potential association with the Scutum-Crux arm is suggested by the proximity of IRAS 16475–4609 to the massive stellar cluster Westerlund 1 ($\ell = 339^\circ 55$, $b = -00^\circ 40$). With a well-constrained distance of 4.05 ± 0.20 kpc ([Navarete et al. 2022](#)), Westerlund 1 lies close enough to suggest that both objects may reside at similar distances, potentially within the same large-scale Galactic structure.

We estimated the mean Lyman continuum photon rate of $N_{\text{Ly}} = 47.36 \pm 0.06$ dex based on hydrogen radio recombination line analysis (Sect. 5.4). The Lyman flux falls below the ionizing flux predicted for an O9–O9.5 V star (47.56–47.90 dex, [Martins et al. 2005](#)), which is consistent with the classification of the near-infrared source as an early B-type star. Furthermore, when applying the calibration of [Vacca et al. \(1996\)](#), the upper limit of the derived flux remains consistent within $\sim 2\sigma$ with a B0–B0.5 V star ($\lesssim 48.0 \pm 0.3$ dex), reinforcing our interpretation.

In addition, the measured extent of the Brackett gamma ($\text{Br}\gamma$) emission in the H II region exhibits a radius of $\sim 16''$ (Fig. 2), corresponding to a projected length of $\sim 0.27 \pm 0.06$ pc at the distance of IRAS 16475–4609. According to the classification scheme outlined by [Kurtz \(2005\)](#), the spatial extent of the ionized gas places IRAS 16475–4609 in a transitional phase between ultra-compact and compact H II regions. This classification supports the interpretation that the source is a relatively young and still-evolving H II region, with the ionized gas closely confined to the vicinity of the central star. Notably, the location of IRAS 16475–4609 at the boundary of a dense sub-millimeter structure places it at a critical interface be-

tween stellar feedback and the surrounding ISM, potentially influencing the next generation of star-forming activity.

ACKNOWLEDGMENTS

We thank the anonymous referee for their constructive comments and suggestions, which helped improve the quality and clarity of this manuscript. The work of FN and SDP is supported by NOIRLab, which is managed by the Association of Universities for Research in Astronomy (AURA) under a cooperative agreement with the National Science Foundation. AD thanks FAPESP and CNPq for continuing support. Based in part on observations obtained at the Southern Astrophysical Research (SOAR) telescope, which is a joint project of the Ministério da Ciência, Tecnologia e Inovações (MCTI/LNA) do Brasil, the US National Science Foundation’s NOIRLab, the University of North Carolina at Chapel Hill (UNC), and Michigan State University (MSU). Based in part on observations made at NSF Cerro Tololo Inter-American Observatory, NSF NOIRLab, which is managed by the Association of Universities for Research in Astronomy (AURA) under a cooperative agreement with the U.S. National Science Foundation. This work has made use of data from the European Space Agency (ESA) mission *Gaia* (<https://www.cosmos.esa.int/gaia>), processed by the *Gaia* Data Processing and Analysis Consortium (DPAC, <https://www.cosmos.esa.int/web/gaia/dpac/consortium>). Funding for the DPAC has been provided by national institutions, in particular the institutions participating in the *Gaia* Multilateral Agreement.

Facilities: SOAR (TripleSpec), CTIO (NEWFIRM)

REFERENCES

- Araya, I., Curé, M., Machuca, N., & Arcos, C. 2023, in IAU Symposium, Vol. 370, Winds of Stars and Exoplanets, ed. A. A. Vidotto, L. Fossati, & J. S. Vink, 180–184, doi: [10.1017/S1743921322004537](https://doi.org/10.1017/S1743921322004537)
- Autry, R. G., Probst, R. G., Starr, B. M., et al. 2003, in Society of Photo-Optical Instrumentation Engineers (SPIE) Conference Series, Vol. 4841, Instrument Design and Performance for Optical/Infrared Ground-based Telescopes, ed. M. Iye & A. F. M. Moorwood, 525–539, doi: [10.1117/12.460419](https://doi.org/10.1117/12.460419)
- Bertin, E., Mellier, Y., Radovich, M., et al. 2002, in Astronomical Society of the Pacific Conference Series, Vol. 281, Astronomical Data Analysis Software and Systems XI, ed. D. A. Bohlender, D. Durand, & T. H. Handley, 228
- Black, J. H., & Dalgarno, A. 1976, ApJ, 203, 132, doi: [10.1086/154055](https://doi.org/10.1086/154055)
- Caratti o Garatti, A., Stecklum, B., Linz, H., Garcia Lopez, R., & Sanna, A. 2015, A&A, 573, A82, doi: [10.1051/0004-6361/201423992](https://doi.org/10.1051/0004-6361/201423992)
- Carpenter, J. M. 2001, AJ, 121, 2851, doi: [10.1086/320383](https://doi.org/10.1086/320383)
- Carpenter, J. M., Snell, R. L., & Schloerb, F. P. 1990, ApJ, 362, 147, doi: [10.1086/169251](https://doi.org/10.1086/169251)
- Csengeri, T., Urquhart, J. S., Schuller, F., et al. 2014, A&A, 565, A75, doi: [10.1051/0004-6361/201322434](https://doi.org/10.1051/0004-6361/201322434)
- Cushing, M. C., Vacca, W. D., & Rayner, J. T. 2004, PASP, 116, 362, doi: [10.1086/382907](https://doi.org/10.1086/382907)
- Dabrowski, I. 1984, Canadian Journal of Physics, 62, 1639, doi: [10.1139/p84-210](https://doi.org/10.1139/p84-210)
- Damineli, A., Almeida, L. A., Blum, R. D., et al. 2016, MNRAS, 463, 2653, doi: [10.1093/mnras/stw2122](https://doi.org/10.1093/mnras/stw2122)
- Gaia Collaboration, Prusti, T., de Bruijne, J. H. J., et al. 2016, A&A, 595, A1, doi: [10.1051/0004-6361/201629272](https://doi.org/10.1051/0004-6361/201629272)
- Gaia Collaboration, Vallenari, A., Brown, A. G. A., et al. 2023, A&A, 674, A1, doi: [10.1051/0004-6361/202243940](https://doi.org/10.1051/0004-6361/202243940)
- Green, J. A., Breen, S. L., Fuller, G. A., et al. 2017, MNRAS, 469, 1383, doi: [10.1093/mnras/stx887](https://doi.org/10.1093/mnras/stx887)
- Groh, J. H., Damineli, A., & Jablonski, F. 2007, A&A, 465, 993, doi: [10.1051/0004-6361:20066401](https://doi.org/10.1051/0004-6361:20066401)
- Hamano, S., Kobayashi, N., Kawakita, H., et al. 2022, ApJS, 262, 2, doi: [10.3847/1538-4365/ac7567](https://doi.org/10.3847/1538-4365/ac7567)
- Hanson, M. M., Conti, P. S., & Rieke, M. J. 1996, ApJS, 107, 281, doi: [10.1086/192366](https://doi.org/10.1086/192366)
- Hanson, M. M., Kudritzki, R. P., Kenworthy, M. A., Puls, J., & Tokunaga, A. T. 2005, ApJS, 161, 154, doi: [10.1086/444363](https://doi.org/10.1086/444363)
- Hanson, M. M., Luhman, K. L., & Rieke, G. H. 2002, ApJS, 138, 35, doi: [10.1086/324073](https://doi.org/10.1086/324073)
- Hou, L. G., & Han, J. L. 2014, A&A, 569, A125, doi: [10.1051/0004-6361/201424039](https://doi.org/10.1051/0004-6361/201424039)
- Israel, F. P. 1978, A&A, 70, 769
- Koornneef, J. 1983, A&A, 128, 84
- Kurtz, S. 2005, in IAU Symposium, Vol. 227, Massive Star Birth: A Crossroads of Astrophysics, ed. R. Cesaroni, M. Felli, E. Churchwell, & M. Walmsley, 111–119, doi: [10.1017/S1743921305004424](https://doi.org/10.1017/S1743921305004424)
- Kwok, S., Volk, K., & Bidelman, W. P. 1997, ApJS, 112, 557, doi: [10.1086/313038](https://doi.org/10.1086/313038)
- Lada, C. J. 1987, in IAU Symposium, Vol. 115, Star Forming Regions, ed. M. Peimbert & J. Jugaku, 1
- Lindgren, L., Hernández, J., Bombrun, A., et al. 2018, A&A, 616, A2, doi: [10.1051/0004-6361/201832727](https://doi.org/10.1051/0004-6361/201832727)
- Lumsden, S. L., Hoare, M. G., Urquhart, J. S., et al. 2013, ApJS, 208, 11, doi: [10.1088/0067-0049/208/1/11](https://doi.org/10.1088/0067-0049/208/1/11)
- Martins, F., Schaerer, D., & Hillier, D. J. 2005, A&A, 436, 1049, doi: [10.1051/0004-6361:20042386](https://doi.org/10.1051/0004-6361:20042386)
- Menten, K. M. 1991, ApJL, 380, L75, doi: [10.1086/186177](https://doi.org/10.1086/186177)
- Mezger, P. G., & Henderson, A. P. 1967, ApJ, 147, 471, doi: [10.1086/149030](https://doi.org/10.1086/149030)
- Minniti, D., Lucas, P. W., Emerson, J. P., et al. 2010, NewA, 15, 433, doi: [10.1016/j.newast.2009.12.002](https://doi.org/10.1016/j.newast.2009.12.002)
- Moisés, A. P., Damineli, A., Figuerêdo, E., et al. 2011, MNRAS, 411, 705, doi: [10.1111/j.1365-2966.2010.17713.x](https://doi.org/10.1111/j.1365-2966.2010.17713.x)
- Mottram, J. C., Hoare, M. G., Lumsden, S. L., et al. 2010, A&A, 510, A89, doi: [10.1051/0004-6361/200913319](https://doi.org/10.1051/0004-6361/200913319)
- Navarete, F., Damineli, A., Ramirez, A. E., Rocha, D. F., & Almeida, L. A. 2022, MNRAS, 516, 1289, doi: [10.1093/mnras/stac2374](https://doi.org/10.1093/mnras/stac2374)
- Reid, M. J., Dame, T. M., Menten, K. M., & Brunthaler, A. 2016, ApJ, 823, 77, doi: [10.3847/0004-637X/823/2/77](https://doi.org/10.3847/0004-637X/823/2/77)
- Reid, M. J., Menten, K. M., Brunthaler, A., et al. 2019, ApJ, 885, 131, doi: [10.3847/1538-4357/ab4a11](https://doi.org/10.3847/1538-4357/ab4a11)
- Russeil, D. 2003, A&A, 397, 133, doi: [10.1051/0004-6361:20021504](https://doi.org/10.1051/0004-6361:20021504)
- Schlawin, E., Herter, T. L., Henderson, C., et al. 2014, in Society of Photo-Optical Instrumentation Engineers (SPIE) Conference Series, Vol. 9147, Ground-based and Airborne Instrumentation for Astronomy V, ed. S. K. Ramsay, I. S. McLean, & H. Takami, 91472H, doi: [10.1117/12.2055233](https://doi.org/10.1117/12.2055233)
- Schuller, F., Menten, K. M., Contreras, Y., et al. 2009, A&A, 504, 415, doi: [10.1051/0004-6361/200811568](https://doi.org/10.1051/0004-6361/200811568)
- Shi, H., Zhao, J.-H., & Han, J. L. 2010, ApJ, 710, 843, doi: [10.1088/0004-637X/710/1/843](https://doi.org/10.1088/0004-637X/710/1/843)
- Skrutskie, M. F., Cutri, R. M., Stiening, R., et al. 2006, AJ, 131, 1163, doi: [10.1086/498708](https://doi.org/10.1086/498708)
- Tenorio-Tagle, G. 1979, A&A, 71, 59

- Turner, J., Kirby-Docken, K., & Dalgarno, A. 1977, *ApJS*, 35, 281, doi: [10.1086/190481](https://doi.org/10.1086/190481)
- Urquhart, J. S., Busfield, A. L., Hoare, M. G., et al. 2007, *A&A*, 461, 11, doi: [10.1051/0004-6361:20065837](https://doi.org/10.1051/0004-6361:20065837)
- Urquhart, J. S., Moore, T. J. T., Schuller, F., et al. 2013, *MNRAS*, 431, 1752, doi: [10.1093/mnras/stt287](https://doi.org/10.1093/mnras/stt287)
- Vacca, W. D., Garmany, C. D., & Shull, J. M. 1996, *ApJ*, 460, 914, doi: [10.1086/177020](https://doi.org/10.1086/177020)
- Walsh, A. J., Hyland, A. R., Robinson, G., Bourke, T. L., & James, S. D. 1995, *PASA*, 12, 186, doi: [10.1017/S1323358000020257](https://doi.org/10.1017/S1323358000020257)
- Walsh, A. J., Hyland, A. R., Robinson, G., & Burton, M. G. 1997, *MNRAS*, 291, 261, doi: [10.1093/mnras/291.2.261](https://doi.org/10.1093/mnras/291.2.261)
- Wegner, W. 2006, *MNRAS*, 371, 185, doi: [10.1111/j.1365-2966.2006.10549.x](https://doi.org/10.1111/j.1365-2966.2006.10549.x)
- Wenger, T. V., Bania, T. M., Balser, D. S., & Anderson, L. D. 2013, *ApJ*, 764, 34, doi: [10.1088/0004-637X/764/1/34](https://doi.org/10.1088/0004-637X/764/1/34)
- Wenger, T. V., Dawson, J. R., Dickey, J. M., et al. 2021, *ApJS*, 254, 36, doi: [10.3847/1538-4365/abf4d4](https://doi.org/10.3847/1538-4365/abf4d4)
- Wood, D. O. S., & Churchwell, E. 1989a, *ApJS*, 69, 831, doi: [10.1086/191329](https://doi.org/10.1086/191329)
- Wood, D. O. S., & Churchwell, E. 1989b, *ApJ*, 340, 265, doi: [10.1086/167390](https://doi.org/10.1086/167390)

APPENDIX

A. COMPARISON BETWEEN TRIPLESPEC/SOAR OBSERVATIONS OF IRAS 16475–4609 AND OB STANDARDS

Figure 11 compares the normalized spectrum of IRAS 16475–4609 with six OB standards with spectral types ranging from O9.5 V to B2 V (from top to bottom). Each panel exhibits useful spectral regions within the near-infrared atmospheric windows covered by the TripleSpec observations.

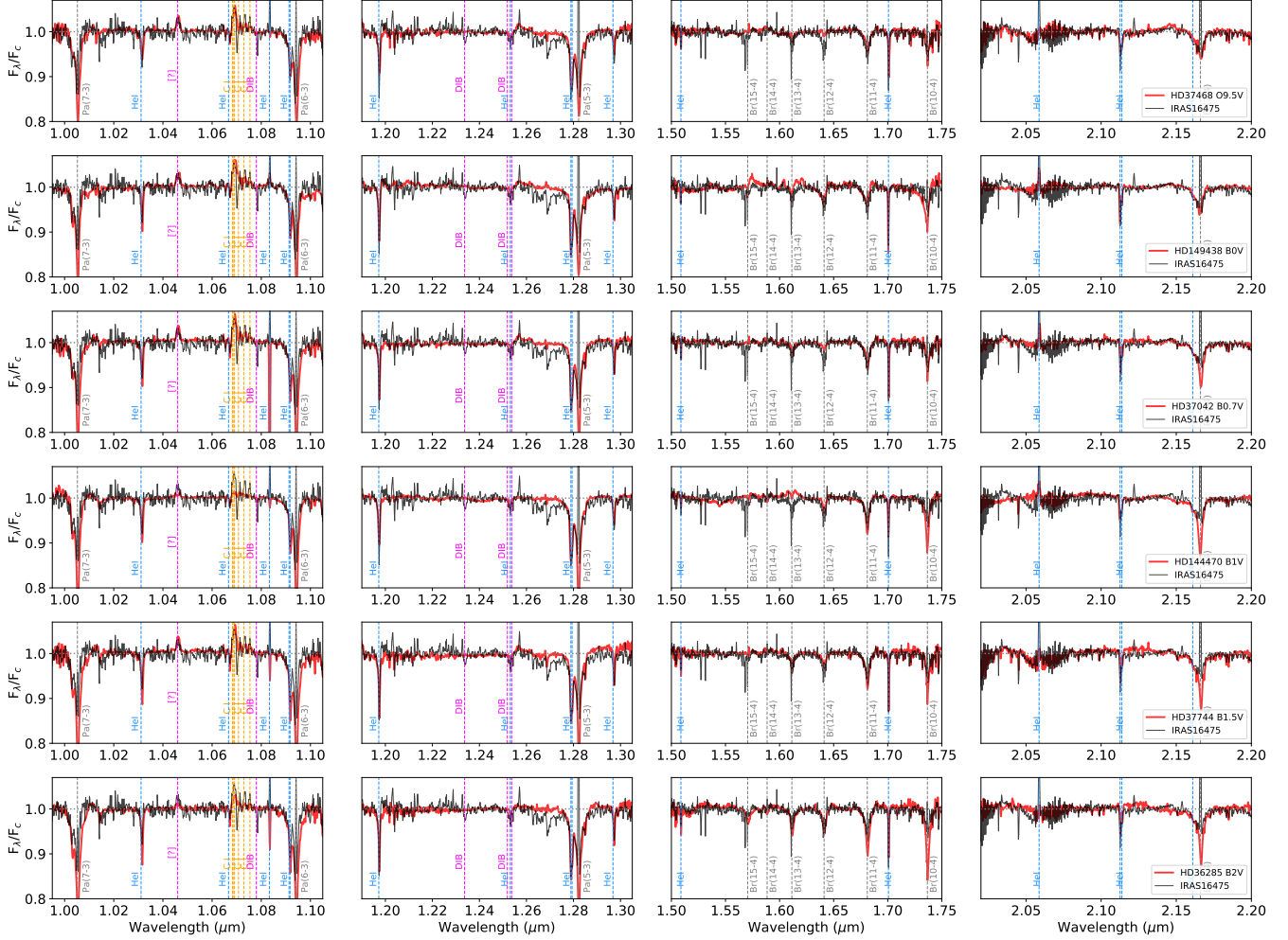


Figure 11. Continuum-normalized TripleSpec spectrum of IRAS 16475–4609 used for spectral type determination. The red curves are a sample of representative OB-type stars observed with TripleSpec (Navarete *et al.*, in prep.), from top to bottom: HD37468 (O9.5 V), HD149438 (B0 V), HD37042 (B0.7 V), HD144470 (B1 V), HD37744 (B1.5 V), and HD36285 (B2 V). The vertical dashed lines indicate H I (grey) and He I (blue) lines used for classification, together with DIB and unknown features (magenta).

The first-row panels present the 1.0–1.1 μm region, delimited by the $\text{Pa}\gamma$ and $\text{Pa}\beta$ lines. Three He I transitions are identified in this region, together with a DIB absorption at 1.078 μm and four unknown emission features in the 1.04–1.08 μm range. In general, the H I and He I lines get stronger towards later spectral types, while the strength of the emission features are only fainter in the spectra of the B1 and B2 V subtypes. The strength of the $\text{Pa}\beta$ at 1.09 μm well-matches the B0 V spectrum.

The second-row panels show the 1.2-1.3 μm window from the J band, containing four He I transitions and the $\text{Pa}\beta$ feature, in addition to a few DIB absorptions. The $\text{Pa}\beta$ and He I $\lambda 12789/94\text{\AA}$ doublet matches the B0 V and B0.7 V spectra.

The third-row panels exhibit the 1.5-1.75 μm region from the H band. Several high-order transitions of the H I Brackett series are located within this region, together with two He I transitions. The higher-order Brackett series are problematic in the comparison spectra, however the first orders are generally reasonably well-sampled. The wings of the H I lines from the IRAS 16475–4609 spectrum are well matched by the B0.7 V star, but also for the earlier O9.5 V.

The forth-row panels exhibit the 2.02-2.20 μm region of the K-band window, containing the $\text{Br}\gamma$ feature and two He I lines. Similarly as observed in the H-band, the wings of the $\text{Br}\gamma$ is consistent with spectral types ranging from O9.5-B0.7 V.